

# Characterization of Ti–6Al–4V Fabricated by Multilayer Laser Powder-Based Directed Energy Deposition

Luis Alexander Ávila Calderón,\* Benjamin Graf, Birgit Rehmer, Torsten Petrat, Birgit Skrotzki, and Michael Rethmeier

Laser powder-based directed energy deposition (DED-L) is increasingly being used in additive manufacturing (AM). As AM technology, DED-L must consider specific challenges. It must achieve uniform volume growth over hundreds of layers and avoid heat buildup of the deposited material. Herein, Ti–6Al–4V is fabricated using an approach that addresses these challenges and is relevant in terms of transferability to DED-L applications in AM. The assessment of the obtained properties and the discussion of their relationship to the process conditions and resulting microstructure are presented. The quality of the manufacturing process is proven in terms of the reproducibility of properties between individual blanks and with respect to the building height. The characterization demonstrates that excellent mechanical properties are achieved at room temperature and at 400 °C.

## 1. Introduction


Industrial production chains use additive manufacturing (AM) technologies increasingly since they offer flexible manufacturing of complex geometries, leading to components with improved functionality. Compared with casting or forming, AM allows tooling cost reduction.<sup>[1]</sup> Therefore, it offers the potential for

L. A. Ávila Calderón, B. Rehmer, B. Skrotzki  
Department of Materials Engineering  
Bundesanstalt für Materialforschung und –prüfung (BAM)  
Unter den Eichen 87, 12205 Berlin, Germany  
E-mail: luis.avila@bam.de

B. Graf, T. Petrat, M. Rethmeier  
Division of Joining and Coating Technology  
Fraunhofer Institute for Production Systems and Design Technology  
Pascalstraße 8-9, 10587 Berlin, Germany

M. Rethmeier  
Department of Component Safety  
Bundesanstalt für Materialforschung und –prüfung (BAM)  
Unter den Eichen 87, 12205 Berlin, Germany

M. Rethmeier  
Institute of Machine Tools and Factory Management  
Technische Universität Berlin  
Straße des 17. Juni, 10623 Berlin, Germany

 The ORCID identification number(s) for the author(s) of this article can be found under <https://doi.org/10.1002/adem.202101333>.

© 2021 The Authors. Advanced Engineering Materials published by Wiley-VCH GmbH. This is an open access article under the terms of the Creative Commons Attribution License, which permits use, distribution and reproduction in any medium, provided the original work is properly cited.

DOI: 10.1002/adem.202101333

time-saving and faster availability of components, which is of high relevance, especially with today's demand for quick market launch. Unlike additive processes with a powder bed, like laser powder bed fusion, which can be used to produce highly complex geometries, powder nozzle-based processes such as laser directed energy deposition (DED-L), also known as laser-metal-deposition (LMD), enable component modification or repair and AM with high build-up rates and multi-layer build-ups.

Titanium alloys like Ti–6Al–4V are widely used in industrial applications. Due to their excellent mechanical properties, low density, and outstanding corrosion resistance and biocompatibility, they find

application in metallic components in medical and dental applications, or in the aircraft sector, e.g., in compressor blades in turbines working at elevated temperature.<sup>[2–4]</sup> Depending on the conditions of the manufacturing process as well as on the characteristics of an eventual posterior thermomechanical treatment, Ti–6Al–4V can feature different microstructural characteristics, which impact their properties significantly.<sup>[2]</sup> The prior  $\beta$  grains' morphology and arrangement of the two phases  $\alpha$  and  $\beta$  are examples of these characteristics. The microstructure of DED-L components is mostly characterized, for instance, by prior  $\beta$  grains with columnar shape.<sup>[4,5]</sup> The two extreme cases of phase arrangement in conventional titanium alloys are the lamellar microstructure and the equiaxed microstructure. Both types of microstructure can have a fine as well as a coarse arrangement of the two phases. The size of the phases (fine or coarse) and their arrangement (lamellar or equiaxed) impact the mechanical properties. These dependencies have been widely studied and are known, for instance, regarding the strength, ductility, creep, and fatigue behavior.<sup>[2,6]</sup>

Titanium alloys pose additional specific challenges during multilayer DED-L since the reaction with atmospheric gases causes unwanted embrittlement. The continuous deposition leads to high substrate temperatures with multiple temperature cycles of heating and cooling, which can potentially originate coarse microstructures. Besides, the lower thermal conductivity of Titanium compared to other metals leads to prolonged cooling durations. These factors contribute to the appearance of embrittlement since the increased temperature means an increased susceptibility for the reaction with atmospheric gases such as oxygen, nitrogen, and hydrogen. The presence of these

atmospheric gases and related embrittlement influences also the mechanical properties of titanium alloys. This influence is well known and described.<sup>[7,8]</sup> Increasing their content usually leads to increased strength and hardness and reduced ductility.<sup>[9,10]</sup>

In multilayer DED-L using powder as feedstock material, single weld beads can be deposited next to each other to cover a whole area with a continuous layer of material. More than a hundred layers on top of each other are quite common. Multiple of these layers form a 3D geometry. Avoiding heat accumulation and thus embrittlement and deterioration of the mechanical properties as well as achieving uniform volume growth are the two main challenges regarding process adjustment, as well as achieving uniform volume growth are the two main challenges regarding process adjustment. The process design for multi-layer DED-L of Ti-6Al-4V must consider these challenges.

There are several studies available that report the mechanical properties of Ti-6Al-4V manufactured by DED-L. These studies investigate different aspects and apply different strategies to deal with these specific challenges. Regarding heat accumulation and embrittlement, Carroll et al. use a process chamber with an argon atmosphere and a second argon gas flow to deliver the powder.<sup>[11,12]</sup> The gas flow is used to provide consistent forced convection conditions throughout processing. Yu et al. and Spranger et al. use instead an argon local shielding gas atmosphere without additional shielding gas devices or a process chamber.<sup>[9,10]</sup> Compared with Yu et al., Spranger et al. use a powder carrier gas in addition to the shielding gas and face the challenge of achieving constant volume growth over hundreds of layers through the optimization of the travel path strategy.<sup>[10]</sup> The combined use of a carrier and shielding gas forms an enhanced local shielding gas atmosphere that will be called from now on a local protective gas atmosphere.

The process chamber used by Carroll et al. leads to a proper shielding gas atmosphere and prevents, therefore, the oxygen-induced embrittlement of the titanium alloy.<sup>[11,12]</sup> In comparison to DED-L in an argon-flooded process chamber (Carroll et al.), the local shielding/local protective gas atmosphere used by Yu et al./Spranger et al. offers the benefit of better accessibility and free movement for the powder nozzle.<sup>[9,10]</sup> Furthermore, there are no size restrictions regarding the substrate. The DED additive build-up can be deposited on existing large components which is of advantage for repair purposes. The DED-L process with local protective gas atmosphere (shielding and carrier gas) has, therefore, become a popular approach. However, compared to a process chamber, a local protective gas atmosphere can only cover a smaller area of the blank. This smaller coverage represents a challenge. Indeed, to avoid oxygen-induced embrittlement, the local protective gas atmosphere must be large

enough to cover the whole susceptible region of high substrate temperature.

The cited studies use different test strategies to assess the obtained mechanical properties. In the study of Yu et al. in the deposition occurs close to the substrate over a small number of layers and a raster deposition pattern including overlap that was rotated 90° between each layer is used.<sup>[9]</sup> To evaluate the tensile properties, they manufacture tensile test pieces horizontally on the substrate plate. For the first few layers of the deposition process, the cold substrate can function as a heat sink due to its cold material mass, and therefore contribute to increasing the cooling rate and confining the area of high surface temperature. Compared with the work of Spranger et al., the deposition of a small number of layers on a cold substrate plate (Yu et al.) does not represent the process conditions during the additive build-up of high structures with hundreds of layers which are targeted in metal AM applications. Carroll et al. manufacture a 100 mm tall cruciform structure consisting of layers of three beads including overlap.<sup>[12]</sup> They test tensile samples oriented perpendicular and parallel to the building direction and located in the bottom and top regions. To evaluate the effect of additional oxygen on the mechanical properties, some regions of the cruciform were exposed to oxygen. The work of Spranger et al. focuses on improving the shielding gas protection and adapting the cooling cycles to control the temperature regime during multilayer deposition.<sup>[10]</sup> Furthermore, they optimize the travel path strategy and achieve uniform volume growth over hundreds of layers. After the manufacturing process, they do not apply any further heat treatment. To roughly determine the achieved properties, they test five tensile samples manufactured from five cylindrical DED-L blanks. **Table 1** shows the mechanical properties of Ti-6Al-4V produced in the three mentioned studies, as well as reference data from the standard for wrought material. The minimum strength requirements are achieved in all studies, but this does not necessarily apply to the elongation at fracture, especially in the study of Yu et al.<sup>[9]</sup> For a fair comparison with the work of Spranger et al., Table 1 shows values from the work of Carroll et al. from tensile samples oriented parallel to the BD and not exposed to oxygen.<sup>[10,12,13]</sup>

The work by Spranger et al. is relevant in terms of transferability to laser metal deposition applications in AM, and its results in terms of mechanical properties are promising.<sup>[10]</sup> Therefore, we follow up on that study by further investigating the obtained properties and process quality. Herein,<sup>[13]</sup> The importance of using a combined flow of shielding and carrier gases to form the local protective gas atmosphere is highlighted and experimentally evaluated to relate the obtained mechanical properties to the process conditions. Furthermore, a

**Table 1.** Mechanical properties for laser deposited Ti-6Al-4V, compared with the standard for wrought material.

Source/method	$R_{p0.2}$ (MPa)	$R_m$ (MPa)	A (%)
DED-L argon-flooded process chamber <sup>[9,10]</sup>	945 ± 13	1041 ± 12	14.5 ± 1.2
DED-L horizontal deposition with high heat dissipation <sup>[9]</sup>	976 ± 24	1099 ± 2	4.9 ± 0.1
DED-L Spranger et al. <sup>[10]</sup>	876 ± 6	923 ± 9	10.1 ± 1.5
DIN EN 3312 for wrought material <sup>[16]</sup>	≥830	900–1160	≥10

characterization and evaluation of the obtained properties and resulting microstructure are presented. Finally, we evaluate the achieved quality in terms of reproducibility of the properties between individual blanks and with respect to the building height. In this study, we do not aim at getting statistically validated characteristic values.

## 2. Experimental Section

### 2.1. Materials

The additively manufactured Ti–6Al–4 V blanks under investigation are fabricated via laser powder-based directed energy deposition (DED-L) with local protective gas atmosphere using the improved shielding + carrier gas protection and the optimized deposition strategy presented by Spranger et al.<sup>[10]</sup> The DED-L blanks are cylinders with 123 mm height and 18 mm target diameter and 240 layers. Five cylinders are built-up in one batch. After the manufacturing process, no further heat treatment is applied. A shell–core strategy like the one used by Montero et al. to achieve near-net shapes is used. **Figure 1** depicts the travel path strategy for a single layer of the DED-L blanks.<sup>[14]</sup> At first, the contour track is deposited along a circular path with a diameter of 17 mm. This track defines the blank boundary. Due to the track width, this leads to a material deposition with a target diameter of 18 mm. In the next step, the inner volume is build-up by parallel tracks next to each other. The track overlap is slightly modified within one layer to ensure constant volume growth. The parallel tracks in the middle of the inner volume feature an overlap ratio of 65%, while the parallel tracks in the outer area are slightly more separated, with an overlap ratio of 42%. The starting points of the contour track and volume tracks are rotated 95° each layer. With a 95° rotation, the starting point of

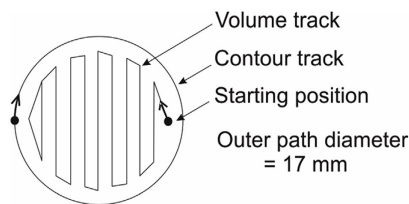


**Figure 1.** Travel path for the cylindrical DED-L blanks.

consecutive layers rotates around the surface, and irregularities during the start of the deposition process are locally distributed and do not add up, as they would with a rotation angle of 90°. The cooling conditions are optimized by adapting the interlayer cooling periods to control the temperature regime during multi-layer deposition. The interlayer cooling period is set to 126 s. The heat tint-free surface is achieved by using a local protective gas atmosphere to carry the powder to the deposition place and by adjusting the inert gas delay times at the endpoints of the volume track. The local protective gas atmosphere uses argon as a shielding gas and helium as a carrier gas. In each contour track a gas delay of 2 s is used, after every core deposition, the inert gas delay is set to 6 s. Further details regarding the manufacturing of the DED-L blanks can be found in the work by Spranger et al.<sup>[10]</sup>

The cylinders are manufactured in a TRUMPF TruLaser Cell 7020 machine (TRUMPF GmbH + Co. KG, Ditzingen, Germany), equipped with a TruDisk 2002 Yb:YAG laser. The 3-jet powder nozzle is positioned by a 5-axis machine. Argon 5.0 is used as shielding gas in all experiments with a flow rate of 10 l min<sup>-1</sup>. The powder material is supplied in a Helium 5.0 gas flow. **Figure 2a)** shows the experimental setup. The substrate plate is made of Ti–6Al–4 V and has a thickness of 25 mm. The design of the three-jet powder nozzle is shown in **Figure 2b)**. The laser beam and the shielding gas are directed through the center of the nozzle. The powder is fed to the weld pool with the carrier gas in three separate jets. These jets are arranged with an angle of 120° along the circumference of the nozzle.

According to the factory certificate, the powder features a spherical grain morphology, and a diameter of 45–105 µm (diameter distribution:  $d_{10} = 51 \mu\text{m}$ ,  $d_{50} = 70 \mu\text{m}$ ,  $d_{90} = 91 \mu\text{m}$ ). The manufacturer of the 3-jet powder nozzle specifies the suitable grain size for this nozzle with a diameter of 45–125 µm. The used powder fits well within this range, being therefore appropriate for the used 3-jet powder nozzle. The applied process parameters are kept for the entire build-up of the cylinders, see **Table 2**.

To assess the mechanical properties of the additively manufactured Ti–6Al–4 V beyond the comparison with available literature data, two batches of conventional material with different processing routes are tested. Two cylindrical bars with diameter of 20 and 35 mm are used (Enpar Sonderwerkstoffe GmbH, Gummersbach, Germany). The material meets the requirements of ASTM B348 Gr. 5 (Standard Specification for Titanium and Titanium Alloy Bars and Billets) and DIN EN 3312 (Aerospace

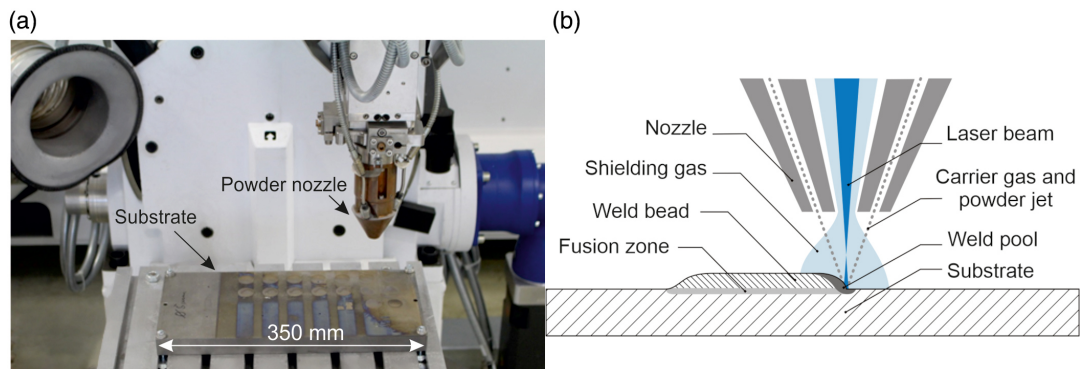


**Figure 2.** a): Experimental set-up of DED-L process and b) design of process nozzle.

**Table 2.** Process parameters for the cylindrical blanks: laser power,  $P$ , spot diameter,  $d$ , welding velocity,  $v$ , mass flow,  $m$ , z-layer increment,  $\Delta z$ , and interlayer cooling period,  $t_{cool}$ .

$P$ (W)	$d$ (mm)	$v$ (mm min <sup>-1</sup> )	$m$ (g min <sup>-1</sup> )	$\Delta z$ (mm)	$t_{cool}$ (s)
1000	1.0	1000	3.8	0.5	126

series—Titanium alloy Ti-6Al-4V).<sup>[15,16]</sup> The material from the two bars was twice vacuum-arc-remelted and subsequently hot-formed, heat treated (solution annealed and aged) and bright ground. The material of the cylindrical bar with 20 mm was used in as-manufactured state. The bar with 35 mm diameter was additionally heat treated to obtain a lamellar microstructure. Relevant literature sources are consulted to choose an appropriate heat treatment strategy.<sup>[2,6,13]</sup> The heat treatment consists of a solution annealing above the  $\beta$  transus temperature at 1050 °C for 1 h with subsequent air cooling to room temperature, followed by aging at 625 °C below the  $\beta$  transus temperature for 4.5 h with subsequent air cooling to room temperature.

## 2.2. Methodology

This work involves two series of experiments. The first one aims to characterize the local protective gas flow and atmosphere and highlight the importance of the use of a shielding gas within the local protective gas atmosphere consisting of shielding + carrier gas. The results are presented and discussed in Section 3.1: First, results from Schlieren measurements, and then, the results of the continuous deposition of three layers, i.e., without cooling time between single layers, with the parameters of Table 2 and the nozzle path of Figure 1.<sup>[17]</sup> The deposition of the three-layers deposition takes place with carrier gas only and with shielding gas + carrier gas. Both strategies are compared and discussed. The analysis of the chemical composition complements this first results, helping to highlight the importance of the use of a shielding gas. Following that first series of experiments, the microstructure, and the mechanical properties of the DED-L blanks and the two investigated variants of conventionally manufactured material are characterized and discussed. The microstructure, as well as the hardness are analyzed at room temperature in the as-built condition in the case of the DED-L material and in the as-manufactured and as-heat-treated condition in the case of the conventional variants. The tensile tests are performed at room temperature and 400 °C.

In the DED-L material, the microstructural and mechanical experiments aim not only to characterize the material but also to demonstrate the achieved quality in terms of reproducibility of the properties between individual blanks and with respect to building height by using a small number of blanks. For this purpose, the five blanks are examined over the height, and the properties (microstructure, hardness, tensile strength) are evaluated in combination: it is known that the hardness is related to the microstructure, also for AM Ti-6Al-4V.<sup>[5]</sup> Besides, the positive correlation between hardness and strength is known and has been already reported for several alloys, including titanium alloys.<sup>[18–20]</sup>

**Table 3.** Cylindrical blanks (1–5) and investigations used for the characterization. T = Top, b = bottom, m = middle.

Blank No.	Investigations										
	Metallography		Tensile RT		Hardness			Density and mass measurement		Tensile 400 °C	
	T	B	T	B	T	M	B	M	T	B	
1	x <sup>a)</sup>	–	–	–	x	–	–	x	–	–	
2	–	–	x	x	x	x	x	–	–	–	
3	–	–	–	–	–	–	–	–	x	x	
4	x <sup>b)</sup>	x <sup>b)</sup>	–	–	–	–	–	–	–	–	
5	x <sup>b)</sup>	–	–	–	–	–	–	–	–	–	

<sup>a)</sup>Qualitative; <sup>b)</sup>Quantitative.

Table 3 shows an overview of the analyzed cylindrical DED-L blanks and the corresponding investigations, including the targeted location to be examined within each blank. On blank No. 1, density and mass measurements are used to calculate the void fraction. The microstructure is characterized based on light microscopy images on three separate cylinders (blanks No. 1, No. 4, and No. 5). Tensile tests are performed on a total of four tensile test pieces coming from the top and bottom of two separate cylinders (at room temperature blank No. 2 and at 400 °C blank No. 3, see Figure 3). Hardness measurements are conducted on the top of blank No. 1 (where the microstructure is qualitatively investigated) and on three residual pieces (threaded region) of the tensile samples coming from blank

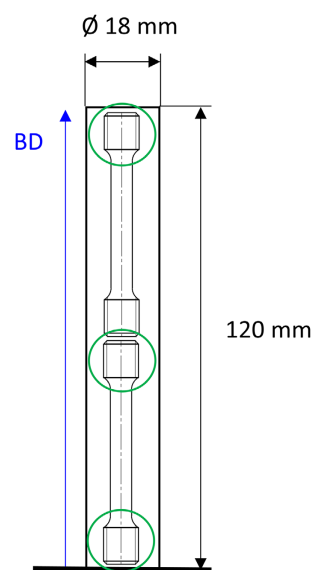


**Figure 3.** Schematic representation of the location of tensile samples within a DED-L cylinder. The green circles represent the threaded regions that were separated for hardness investigations after tensile testing. (BD: Building Direction; total length of cylinder: 120 mm; total length of tensile test piece: 60 mm).

No. 2 corresponding to bottom, middle, and top regions of the cylindrical blank (see Figure 3).

### 2.3. Chemical Composition, Microstructure, and Hardness

The composition of the powder used to manufacture the DED-L material is given by the factory certificate. For the bulk material, Al, V, and Fe were determined with an optical emission spectrometer (OES). O, N, and H were identified using carrier gas hot extraction. For the determination of H a coupled quadrupole mass spectrometer was used. C was determined with combustion analysis. The chemical composition of the DED-L material was determined from samples manufactured from the middle region of one blank with a width of 5 mm (blank not listed in Table 3).

To study the microstructure, samples are cold mounted and subsequently ground in three steps using resin-bonded diamond discs (MD Piano, Struers GmbH, Germany), with a surface finish number ranging from 220 up to 1200. Finally, they are mechanically polished, including the usage of a 0.2  $\mu\text{m}$  suspension (90% OPS and 10%  $\text{H}_2\text{O}_2$ , PT Chem, Cloeren Technology GmbH, Germany) in the last step. Etching occurs for 15–20 s using Kroll's reagent. The samples are investigated using an optical microscope (Zeiss Axiotech 100 HD, Carl Zeiss Jena GmbH, Germany), and an inverted metallurgical microscope GX71 (Olympus Europa SE & CO. KG, Hamburg, Germany). The size of the defects, as well as additional microstructural features are measured using ImageJ 1.52p.<sup>[21]</sup> The fractured tensile test pieces are investigated with a light microscope Keyence VHX-2000 (KEYENCE Deutschland GmbH, Germany).

The void fraction of the material, i.e., closed porosity including lack of fusion defects, is determined using the material's mass and density. It is determined as the ratio in percentage between the volume of voids in the AM sample to its entire volume. The volume of the voids was approximated as the difference between the volume of the AM sample and its approximate fully dense volume. The fully dense volume was approximated as the ratio between the mass of the AM sample and the average fully dense reference density of the two disks of conventional material. This approach to calculating the closed porosity represents a good and faster alternative to methods such as microcomputed tomography and image processing and analysis. The mass is determined using a balance Sartorius BSP210D (Sartorius AG, Germany) and the density using a balance Sartorius MC 410S and the Archimedes' principle according to DIN EN ISO 1183-2.<sup>[22]</sup> The reference liquid is *n*-heptane. In total, five mass measurements and three density measurements are performed on one half-cylinder coming from the bottom of the DED-L blank No. 1. And on disks of the conventional variants.

To measure the hardness, small load Vickers hardness measurements (HV1) are performed according to DIN EN ISO 6507-1:2018-07 on surfaces perpendicular and parallel to the building direction.<sup>[23]</sup> A calibrated automatic hardness tester (Model: KB 30 SR FA Basic, from KB Prüftechnik GmbH, Germany) is used. HV1 is used to minimize possible scatter due to the finest microstructural features. To select HV1, the expected diagonal indentation length is estimated and then compared with the

microstructure of the investigated samples. All investigated samples are mechanically polished until 3  $\mu\text{m}$ , after that, they are electrolytically polished, using electrolyte A3 (Struers GmbH, Germany) and 35 V for 10–30 s.

The indentation pattern used in blank No. 1 (see Table 3) is a line with a 300  $\mu\text{m}$  distance between indentations. The threaded regions are mechanically cut through the middle to investigate surfaces parallel and perpendicular to the building direction. They are located at the bottom, center, and on the top region of the cylinder (see Figure 3). The indentation pattern is a line with a 250  $\mu\text{m}$  distance between indentations in the surfaces perpendicular to the building direction, and a  $6 \times 5$  indentation matrix with a 1 mm distance between indentations on the surface parallel to the building direction. In the conventional samples, the indentation pattern is a  $6 \times 6$  indentation matrix with a 1 mm distance between indentations.

### 2.4. Tensile Testing

The alloy Ti–6Al–4V was initially developed for aerospace applications with temperatures that did not exceed 350 °C and is stable at temperatures up to 400 °C.<sup>[6]</sup> Data sheets of manufacturers of this alloy, reference books and databases usually report typical characteristic values of high-temperature strength up to about 500 °C.<sup>[6,24]</sup> This help designers to dimension critical parts and components. However, it is common practice in open literature to report only data at room temperature, such as the one listed in Table 1 as a first approach to assess the mechanical behavior. Given their relevance for design, the present study goes beyond that and reports also high-temperature strength values.

To characterize the DED-L material, two cylindrical tensile samples are used (see Table 3). From each cylinder, two tensile samples are manufactured; one from the top and one from the bottom region (see Figure 3). To characterize the conventional variants, three tensile samples of each variant are tested per temperature. The load direction coincides in the DED-L tensile samples with the building direction (BD) and in the conventional material with the forming direction (FD). The tensile samples used are B  $6 \times 36$ , according to DIN 50 125 (thread M10, total length 60 mm, diameter of parallel length 6 mm, parallel length 36 mm).<sup>[25]</sup> The tensile tests are conducted at room temperature according to DIN EN ISO 6892-1 and at 400 °C according to DIN EN ISO 6892-2.<sup>[26,27]</sup> A 100-kN Instron testing machine (Model: 4505, Instron GmbH, Germany, class 1 calibration) is used.

At room temperature and 400 °C, the tensile tests are carried out strain-rate-controlled. The strain rate is kept constant up to and including the determination of the yield strength. Subsequently, the extensometer is removed, and the test continued crosshead-speed-controlled until failure. At room temperature, the strain rate is 0.00025  $\text{s}^{-1}$  up to 1.2% engineering strain, and an extensometer system HBM DD1 is used (Hottinger Brüel & Kjaer GmbH, Germany, class of extensometer 0.2). After that, the crosshead speed is 0.24  $\text{mm s}^{-1}$ . At 400 °C, on the other hand, the strain rate is 0.00007  $\text{s}^{-1}$  up to 1.5% engineering strain, and an MTS (MTS Systems GmbH, Germany, Model: 632.51C-05, class 1) water-cooled high-temperature extensometer is used. After that, the crosshead



speed fitted the recommended strain rate range of method A of the standard.

### 3. Results and Discussion

#### 3.1. Role of Combined Use of Shielding and Carrier Gas Flow to Form the Local Protective Gas Atmosphere

The results of the Schlieren measurement are presented in **Figure 4**.<sup>[17]</sup> This measurement allows for an optical evaluation of the gas coverage of the surface and the turbulent or laminar flow characteristics. **Figure 4a** shows the shielding gas flow through the powder nozzle. The argon shielding gas leads to laminar flow, which spreads over the surface of the blank. **Figure 4b** shows the helium carrier gas flow. There is less gas coverage of the surface in **Figure 4b**, which indicates a worse shielding of the surface by the carrier gas compared with the shielding gas. Using a shielding gas flow in addition to the carrier gas flow is meaningful since it increases the gas coverage of the surface. The combination of both gas flows is shown in **Figure 4c**. The carrier gas flow causes a constriction of the shielding gas flow. Slight turbulence is visible. The gas coverage of the surface is better than in **Figure 4b**. Instead of argon, helium is used as carrier gas because with its density of  $0.1785 \text{ kg m}^{-3}$ , it is much lighter than argon (density  $1.784 \text{ kg m}^{-3}$ ). Due to its low density, the helium carrier gas jet leads to less disturbance, and therefore, less turbulence of the center shielding gas flow compared with an argon carrier gas jet.

For cost optimization of the deposition process, the question might arise whether it could be possible to apply a deposition process with the carrier gas only. While the results of the Schlieren measurement (**Figure 4**) already indicate that it is necessary to use the combined flow of shielding gas and carrier gas, the practical deposition experiment further confirms this, as seen

in **Figure 5**. **Figure 5a** shows the blank deposited with the carrier gas only. The evaluation of the heat tint provides a good indication of whether the local protective gas atmosphere can successfully prevent the reaction with atmospheric gases; a blue heat tint indicates the reaction with atmospheric gases, and therefore the low protective effect of the carrier gas flow.<sup>[28]</sup> Furthermore, the deposition process is not stable, leading to an uneven surface and defects between the circular contour track and the inner volume tracks. **Figure 5b**, deposited with carrier and shielding gas, shows a more even surface. Only a slight golden heat tint is visible. This result clearly demonstrates that a better shielding to atmospheric gases during the welding process is achieved by using the combined gas flow shown in **Figure 4c**.

**Figure 6** shows an example of the investigated cylindrical blanks built using the combined gas flow shown in **Figure 4c**. Along the contour track, the heat dissipation is lower, while, at the time, the shielding gas coverage is short. Therefore, heat tint is visible along the contour of the blanks, indicating a reaction with atmospheric gases. Along the height of the specimen, the heat tint pattern seems periodic. A possible explanation for this behavior is the  $95^\circ$  rotation of the starting point of each contour track. As explained above, this is done to distribute irregularities during the start and the end of the contour track deposition process. The heat tint changes also along the contour track (**Figure 6**, right). Therefore, the constant starting point rotation after each layer could lead to the heat tint pattern.

The contour track is necessary, as it allows achieving a good net-shape build-up process. The bulk is the one that must provide proper mechanical properties. The surface of the inner-volume layers (**Figure 6**, right) is bright, without heat tint. The shielding gas coverage was sufficient along the inner volume tracks. In contrast to the continuous 3-layer deposition without cooling break between layers in **Figure 5b**, the five cylinders in **Figure 6**

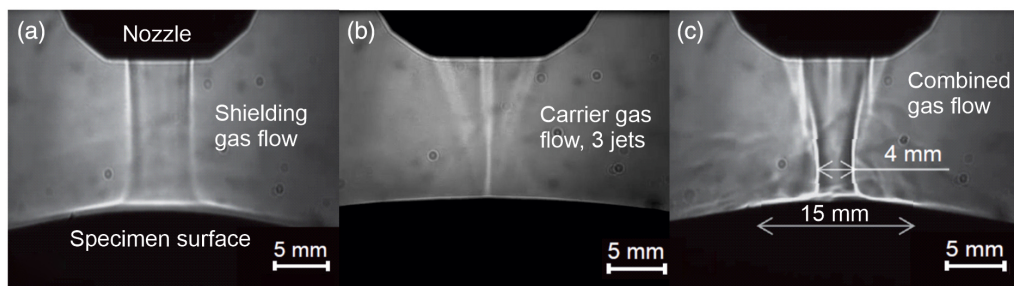


**Figure 4.** Results of Schlieren measurements of a) shielding gas, b) carrier gas, and c) combined shielding and carrier gas.

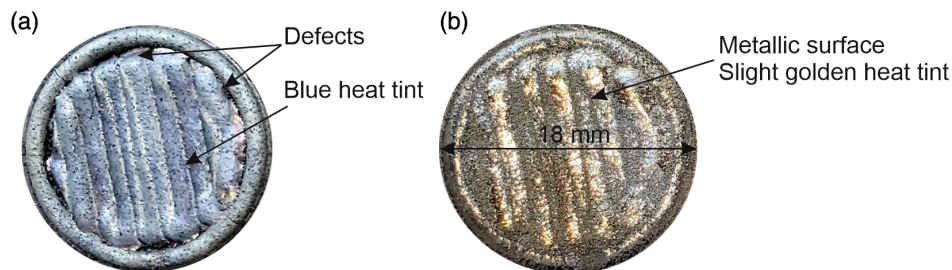


**Figure 5.** Deposition of three layers on the substrate plate, a) carrier gas only, and b) combined shielding and carrier gases.

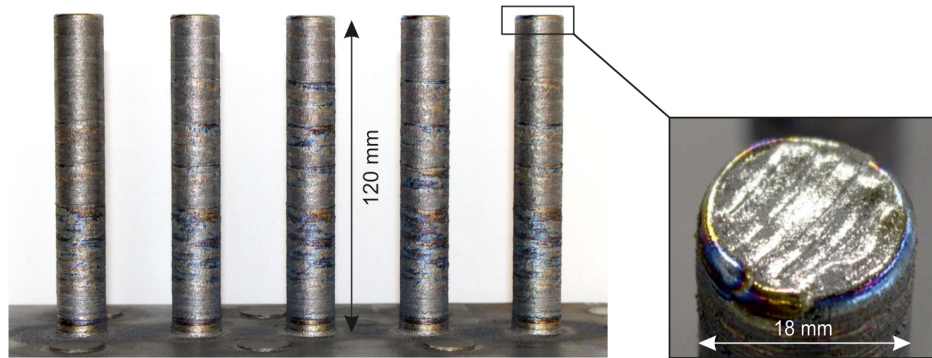


**Figure 6.** Left: as-built cylindrical blanks, 240 layers, right: no heat tint on the surface of the inner volume layers, heat tint only along the contour track. The photograph on the left is reproduced from the work of Spranger et al., with the permission of the Laser Institute of America.<sup>[10]</sup>

are manufactured in one batch. This means that one layer is deposited on each cylinder before the deposition continues with the next layer for the first cylinder. The pause in the deposition process between single layers allows for heat dissipation. This heat dissipation reduces the susceptibility to the reaction with atmospheric gases and is the reason why the inner volume of the blanks in Figure 6 has less heat tint compared to the welded blank in Figure 5b.

**Table 4** summarizes the analyzed chemical composition of the materials investigated along with the maximum values specified for this alloy according to ASTM B348.<sup>[16]</sup> The chemical composition of the Ti–6Al–4 V powder material and of the conventional variants (as-manufactured, heat-treated) is given by the factory certificate. The composition of the cylindrical DED-L blanks was determined within this study as described in Section 2. The limit for the oxygen content in additively manufactured components is given by Yan et al. with 0.22 wt% up to 0.4 wt%, depending on the microstructure.<sup>[29]</sup> This is comparable to the threshold given by ASTM B 348 (see Table 4). The measured values in our DED-L material are lower than the maximum values specified in the standard and in the work by Yan et al. for all measured elements including oxygen and nitrogen. This result proves qualitatively the effectiveness of the use of a combined flow of shielding and carrier gases within the local protective gas atmosphere and complements the results discussed so far.

### 3.2. Microstructure

#### 3.2.1. DED-L Material

**Figure 7, 8 and 9** show different microstructural features of the DED-L material. Sections parallel (Figure 7, left) and

perpendicular to the building direction (BD) (Figure 7, right) are analyzed. Figure 7 illustrates an overview of the etched microstructure. Figure 8 includes micrographs of the microstructure and highlights the existing defects (black regions). Figure 9 shows the microstructure at higher magnification. The melt pool boundaries are visible in both micrographs of Figure 7. They correlate with the travel path strategy. Noteworthy is the fill-contour transition region, which can be identified on both micrographs (marked by arrows). Furthermore, one can also distinguish the pendulum deposition strategy in the core region (Figure 7, right) and the layer-wise build-up strategy (Figure 7, left). The grain morphology is anisotropic and consists of elongated grains featuring different widths. The grains grow in the building direction, are separated by prior  $\beta$ -grain boundaries (marked by arrows) and extend over multiple layers. This suggests epitaxial growth of  $\beta$  grains by nucleation on the underlying layer, combined with a remelting and solidification process.<sup>[5]</sup> Inside the prior  $\beta$  grains, the microstructure is needle like (Figure 9) and organized in different orientations. In Figure 9, the optical microscopy nearly reaches its limit in terms of resolution due to the very fine nature of the needles. Note that, the prior  $\beta$  grain boundaries are free of any  $\alpha$  phase. The acicular microstructure, also reported by other authors, is formed as a result of the fast cooling rates from the  $\beta$  region, which for DED-L are between  $10^3$  and  $10^4$  K s<sup>-1</sup>.<sup>[4,30]</sup> The fast cooling rates from the  $\beta$  region result in the martensitic formation of the  $\alpha'$  phase.<sup>[5,31]</sup> Its formation generally requires sufficiently high cooling rates combined with substrate temperatures in the AM process which are lower than the martensite start temperature,  $M_s$ . This means that the temperature of the build plate or any underlying layer for the further deposition must be lower than  $M_s$ . Otherwise, no martensite transformation will take place during cooling of

**Table 4.** Chemical composition of Ti–6Al–4 V powder material, cylindrical blanks, and conventional variants (as-manufactured and heat treated) in wt%.

	Al	V	Fe	O	N	C	H	Others	Ti
Powder	6.24	4.06	0.19	0.12	0.005	0.005	0.003	–	bal.
DED-L	6.1	3.9	0.18	0.17	0.017	0.012	0.0003	–	bal.
As-manufactured	5.98	4.04	0.149	0.16	0.008	0.018	0.001	<0.4	bal.
Heat treated	6.16	4.13	0.156	0.17	0.009	0.013	0.001	<0.4	bal.
Max. values ASTM B348 <sup>[16]</sup>	6.75	4.5	0.40	0.20	0.05	0.08	0.015	0.4	bal.

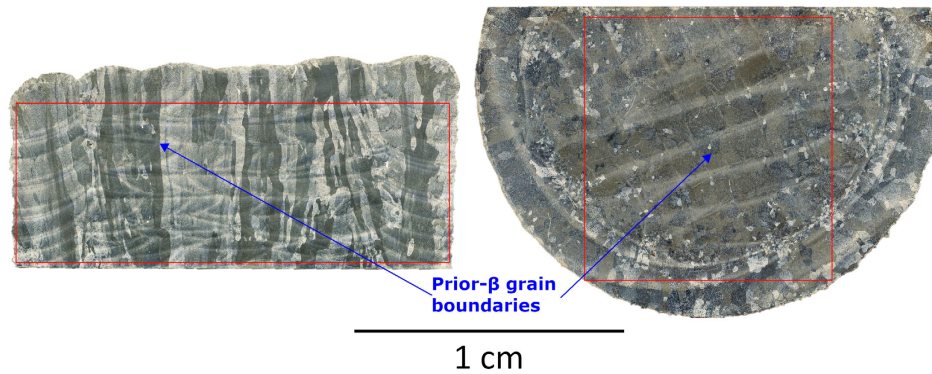


**Figure 7.** Overview of the etched microstructure, left: surface parallel to BD; right: surface perpendicular to BD. The red rectangles depict the regions used for the microstructure analysis (see results in Table 5) (Kroll's reagent, optical microscopy). The prior  $\beta$  grains have an elongated morphology in BD and appear in different shades of gray.

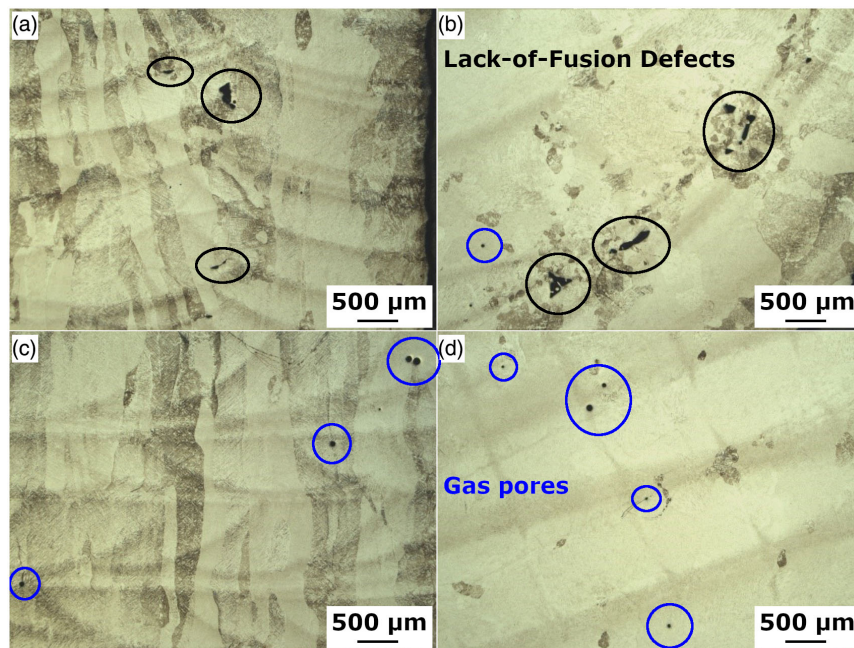


**Figure 8.** Visualization of typical defects found in the cylindrical blanks: a) and b): transition region a) parallel to BD and b) perpendicular to BD. c,d) Center region c) parallel to BD and d) perpendicular to BD. (Kroll's reagent, optical microscopy).

the deposited layer. There are varying values given for  $M_s$  in the literature (between 575 and 800 °C) due to, e.g., different initial microstructures and local chemical inhomogeneities.<sup>[5]</sup> These temperatures are achieved in our process thanks to the chosen interlayer cooling periods and confirmed by the microstructure results of this study. Ahmed et al. have shown that martensite forms in Ti-6Al-4V once the cooling rate exceeds  $410 \text{ K s}^{-1}$  which is the case in the DED-L process.<sup>[31]</sup> Liu et al. developed a model for laser direct deposition and demonstrated that this requirement is fulfilled even in the heat-affected zone, which reached a cooling rate of about  $5 \times 10^3 \text{ K s}^{-1}$ .<sup>[5]</sup> Therefore, although we did not perform transmission electron microscopy or X-ray diffraction investigations in this study, it can be

reasonably assumed that the acicular phase is not the  $\alpha$  but the martensitic  $\alpha'$  phase (both with hexagonal crystal structures).

The two planar sections visible in Figure 7 were used to make a quantitative characterization of the microstructure of the DED-L material. Table 5 summarizes the results together with the results of the two conventional variants, which are presented and discussed in Section 3.2.2. The average prior  $\beta$  grain size and the mean lineal intercept values ( $\bar{l}$ ) were calculated according to ASTM E112-13 and DIN EN ISO 643:2013-05 applying the line-cutting method.<sup>[32,33]</sup> The distance between the cutting lines was 0.7 mm. Due to the anisotropy of the microstructure, one cannot determine a generally valid average grain size. Instead, according to ASTM E112-13, one can calculate the vertical and



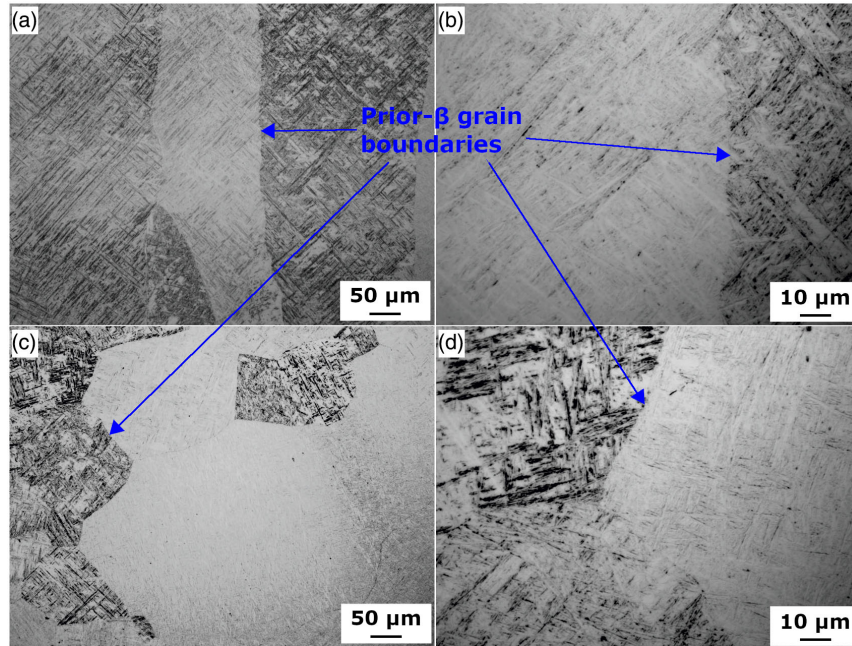


**Figure 9.** Detailed optical images of lamellar microstructure. a,b) parallel to BD, c,d) perpendicular to BD (Kroll's reagent, optical microscopy).

**Table 5.** Microstructure parameters of the three tested variants of Ti–6Al–4V.

	Unit	DED-L <sup>a)</sup>			Equiaxed <sup>a)</sup>			Lamellar <sup>a)</sup>
		TL	T		TL	T	CL    FD	
		CL ⊥ BD	CL    BD		CL ⊥ FD	CL    FD		
$\bar{l}$	mm/i	0.529	2.091	0.521	0.009	0.023	0.007	0.899
G	–	–	–	–1... –2	–	–	11	–2... –3
AI	–	3.9	–	–	2.6	–	–	–

<sup>a)</sup>BD = build direction, FD = forming direction, T = transverse section, TL = tangential longitudinal section, CL = cutting lines, ⊥ = perpendicular to, || = parallel to, mm/i = mm per intersect.

horizontal mean lineal intercept values ( $\bar{l}$ ) in the surface parallel to BD (Figure 7, left) and, as the ratio between them, the anisotropy index (AI).<sup>[32]</sup> Also, one can estimate the average grain size for the surface perpendicular to BD (Figure 7, right), where the grains appear equiaxed. The grain size number, G, might, however, not be a representative value for this grain morphology due to its broad size distribution, where the mean lineal intercept values range from around 50 μm up to 3 mm. The horizontal mean lineal intercept value in the surface parallel to BD, and the mean lineal intercept value in the surface perpendicular to BD are similar and can be interpreted as the average width of the columnar grains. The anisotropic grain morphology of the DED-L material has been already reported for Ti–6Al–4V produced by DED-L and is better recognizable on a surface parallel to the BD (see left side of Figure 7).<sup>[30]</sup> However, on a surface perpendicular to the BD (see right side of Figure 7), the prior β grains appear as partially equiaxed with a broad size distribution; there are colonies of grains with small grain sizes located either next to or within bigger grains. This feature has not been reported in

the literature and could be related to the travel path strategy used in the investigated blanks. The width of the needles in the DED–L material is quite small, on average  $0.7 \pm 0.2 \mu\text{m}$  (138 measurements). The value must be taken with caution since it lies near to the resolution limit of the optical microscopy. The further investigations of the microstructure that were done only qualitatively (blanks Nos. 4, and 5 in Table 3) reveal that there are no differences regarding grain morphology and subgrain structure, unlike the results reported by Carroll et al.<sup>[12]</sup> This unique result is further discussed in combination with the results of hardness and tensile strength in Sections 3.3 and 3.4.2 regarding the reproducibility of the process.

Regarding defects, the sample has gas entrapment porosity and lack of fusion defects, which can be identified in Figure 8. Lack of fusion defects with irregular shapes, including sharp edges, are the biggest defects and are, within the analyzed region, predominantly located in the fill-contour transition region, see Figure 8a,b. Furthermore, gas porosity is seen, principally in the fill region from which the tensile samples come, but

also in regions near the fill-contour transition region. The number of defects is very small and the void fraction, i.e., closed porosity, is 0.09%. This value includes lack of fusion voids, and it was calculated based on one half-cylinder coming from the bottom of blank No. 1. The determined density for the DED-L material is  $4.404 \text{ g cm}^{-3}$ . In the plane of analysis, the lack-of-fusion defects (see Figure 7) feature a maximum Feret diameter ranging from 21 up to  $\approx 446 \mu\text{m}$ , with an average of  $114 \mu\text{m}$ , while the round pores' diameter ranges from 10 up to  $94 \mu\text{m}$ , with an average of  $39 \mu\text{m}$ . The maximum Feret diameter is determined as the largest distance between two parallel planes restricting the defect shape perpendicular to the direction of measurement.

The optimized travel path strategy and shielding strategy led to a very low defect population in the fabricated DED-L material (bulk density  $>99\%$ ). Therefore, the impact on tensile properties should be negligible, as there is no significant reduction in the load-bearing area. The gas entrapment porosity and lack of fusion defects, which can be identified in Figure 8 are both common defects in AM microstructures.<sup>[4]</sup> The round porosity is attributable to two typical causes if considering the specified powder size and diameter distribution ( $d = 45\text{--}105 \mu\text{m}$ ;  $d_{10} = 51 \mu\text{m}$ ,  $d_{50} = 70 \mu\text{m}$ ,  $d_{90} = 91 \mu\text{m}$ ) and the pore's dimensions presented before (diameter ranging from  $10 \mu\text{m}$  up to  $94 \mu\text{m}$ ,  $39 \mu\text{m}$  average). First cause can be the entrapment of alloy vapors generated inside the molten pool of either the carrier or the shielding gas, and second, the entrapment of gases inside the powder particles during the powder manufacturing process.<sup>[4]</sup> At this point, no further differentiation is made, as the impact on the evaluated tensile properties is estimated to be low. Lack-of-fusion voids are predominantly located in the fill-contour transition region. In this specific case, this conflicts with two facts:

first, Ti-6Al-4V is less susceptible to the formation of these types of defects than other typical AM alloys, as shown by Mukherjee et al., and second, the process parameters (see) lie within the optimal processing region that was reported by Dass et al.<sup>[36,37]</sup> The optimized DED-L deposition did not lead in this case to a lack-of-fusion-defect free volume. A possible explanation for it is that in that region, the circular contour track overlaps with the straight parallel tracks of the inner volume (see Figure 1, 5, and 7 right), leading to an uneven track overlap. Therefore, that area becomes more susceptible to defects. The presence of lack-of-fusion voids primarily in the fill-contour transition region has recently been reported for this alloy printed by the LMD process by Chioibasus et al.<sup>[36]</sup> There, the authors attribute it to an offset between contour and meander. The offset, i.e., insufficient track overlap that is highlighted there might also occur in some regions of our samples as explained above. Lack-of-fusion voids primarily in the fill-contour transition region have also been reported for this alloy printed by the laser powder bed fusion (LPBF) process, and for the alloy system IN718 manufactured by DED-L; there, being rather related to the variation of process parameters.<sup>[37-39]</sup> A further optimization strategy, e.g., based on either locally increasing the track overlap or optimizing the process parameter could help to overcome this issue.

### 3.2.2. Conventional Material

The microstructure of the conventional variants is presented in Figure 10 and the results of the corresponding quantitative analysis in Table 5. Figure 10a shows the microstructure of the as-manufactured Ti-6Al-4V parallel to the rod's axis, Figure 10b perpendicular to it. Figure 10c,d illustrates the

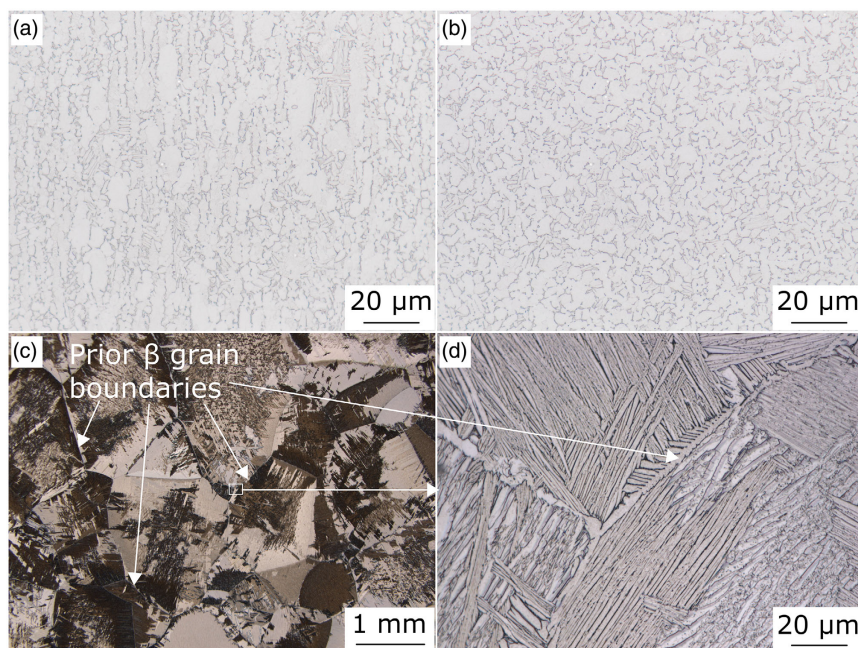


**Figure 10.** Micrographs showing the microstructure of the conventional variants used to benchmark the DED-L Ti-6Al-4V. a,b) equiaxed microstructure of the as-manufactured Ti-6Al-4V a) parallel to the rod axis and b) perpendicular to it. c,d) lamellar microstructure of the heat-treated Ti-6Al-4V (parallel to forming direction) with c) lower and d) higher magnification, the prior  $\beta$  grains have an equiaxed morphology.

microstructure of the heat-treated Ti–6Al–4 V parallel to the forming direction with lower and higher magnification, respectively. The as-manufactured material features an equiaxed microstructure that is elongated in the forming direction, as visible in Figure 10a,b. The appearance of the equiaxed microstructure is rather fine. Small amounts of  $\beta$  phase (darker gray) are present. The equiaxed microstructure is a product of the hot forming process and subsequent solution annealing and aging during fabrication.<sup>[2]</sup> The  $\beta$  phase appears as a narrow fringe around the bright-appearing equiaxed  $\alpha$ .<sup>[2]</sup> The heat-treated material has an equiaxial prior  $\beta$  grain structure. Therefore, only micrographs parallel to the rod axis are shown as considered representative. The higher magnification reveals the existence of a basketweave microstructure with  $\alpha$ -lamellae packages organized in different orientations within the prior  $\beta$  grains. It represents the typical microstructure after slow cooling from the  $\beta$  phase field ( $\beta$  annealed) where the  $\alpha$  phase forms as Widmannstätten laths within the  $\beta$  grains.<sup>[40]</sup> The cooling rate determines the lath size, and the basketweave morphology forms when cooling rate is slow. The grains and lamellae are separated by small amounts of  $\beta$  phase (dark regions in Figure 10e).<sup>[2]</sup> Compared with the images in Figure 9, the lamellar microstructure of the conventional variant, Figure 10d, is coarser than the one of the DED-L material. In Figure 9 and 10c, the different colors within the prior  $\beta$  grains are due to different orientations of the  $\alpha$  lamellae during its formation. The slower cooling rate through air cooling from the heat treatment compared with the DED-L process led to thicker  $\alpha$  lamellae. The average width of the lamellae is  $1.5 \pm 0.9 \mu\text{m}$  (145 measurements), and the size distribution is right-skewed.

### 3.3. Hardness

Table 6 shows the average hardness from the threaded regions of the tensile samples from blank No. 2 (see Table 3). It was determined to investigate the variation of hardness with respect to the building direction. The analyzed threaded regions were located on the top, middle, and bottom positions of the blank (see green circles in Figure 3). Between each of the analyzed surfaces (parallel and perpendicular to BD), no significant differences in the hardness values were found. Therefore, each hardness value reported in Table 6 is the average of the measurements made in both analyzed surfaces (parallel and perpendicular to the building direction).

The results shown in Table 6 indicate that there is no significant variation of the hardness along the building direction. This finding points to a homogeneous microstructure along the building direction, supporting the results of the metallographic investigations. Besides, a comparison between the values obtained in

**Table 6.** Results of hardness measurements along the build-up direction of blank 2.

	Average hardness HV1	Uncertainty of measurement $\pm$
Top	346	9
Middle	363	10
Bottom	349	10

Table 6 with the obtained hardness from blank No. 1,  $362 \pm 10 \text{ HV1}$ , reveals that there is no significant variation of hardness between two different blanks (nos. 1 and 2).

The hardness of the as-manufactured conventional variant with equiaxed microstructure is  $311 \pm 14 \text{ HV1}$  in the cross section and  $338 \pm 14 \text{ HV1}$  in the longitudinal section ( $325 \pm 14 \text{ HV1}$  considering all indentations). In the case of the heat-treated conventional variant with lamellar microstructure, it is  $347 \pm 16 \text{ HV1}$  (longitudinal section). The uncertainty of measurement was calculated according to DIN EN ISO 6507-1 Appendix D.<sup>[23]</sup>

The gradual increase in hardness values between the three variants can be related to the degree of fineness of the respective microstructures. The DED-L material features more similar hardness values compared to the conventional heat-treated variant with lamellar microstructure than compared to the conventional as-manufactured variant with equiaxed microstructure. The finer needle like substructure containing  $\alpha'$  phase can explain this tendency. All hardness values reported in this study are in good agreement with available comparison data. Neither ASTM B348 nor DIN EN 3312 establish a requirement for the hardness value of this alloy.<sup>[15,16]</sup> Equivalent studies on DED-L Ti–6Al–4 V in the literature in terms of extent, low uncertainty of measurement, and amount of hardness indentations are unknown to the authors. Nevertheless, some studies have reported some similar hardness values from as-built LPBF Ti–6Al–4 V in the range of 354–407 HV.<sup>[41–43]</sup> A manufacturer gives as typical for the hardness of the conventional material values from 330 to 390 HV.<sup>[24]</sup>

### 3.4. Tensile Properties

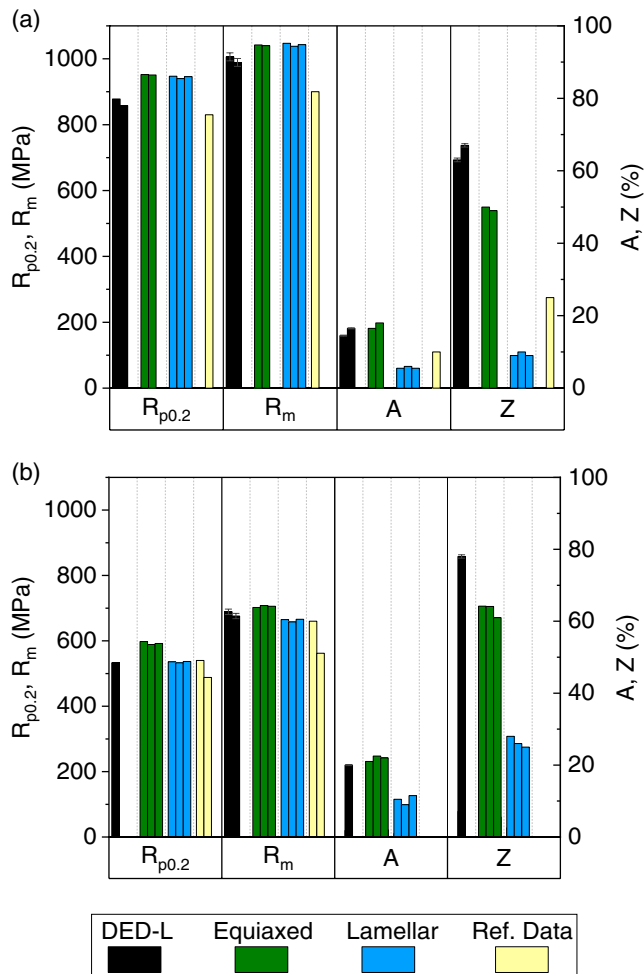
#### 3.4.1. Characteristic Values and Fracture Behavior

Figure 11 summarizes the characteristic values obtained from the tensile tests for all tested variants. The conventional variants are named according to their respective characteristic microstructural feature (as-manufactured = equiaxed, as-heat-treated = lamellar). At room temperature, the reference data comes from the standard DIN EN 3312.<sup>[15]</sup> At 400 °C from a manufacturer's datasheet and the work by Kim et al.,<sup>[24,44]</sup> Figure 11 also contains reference data for comparison, and the uncertainty of measurement from the characteristic values obtained for the DED-L material (error bars in gray), which will be discussed in the context of reproducibility of the process in the following paragraph. The single values are available in Table S1, Supporting Information. Figure 12 shows representative stress–strain curves. For a clearer presentation of the results, the curves are plotted only up to the strain level at which the control mode at room temperature changed to displacement control and the strain rate increased.

The strength and deformation characteristic values of the DED-L material (Figure 11) comply with the specification in the standard for wrought material at room temperature and are comparable with the comparison data of conventional material at 400 °C. Especially, the elongation after fracture ( $A$ ) and the reduction of area ( $Z$ ), i.e., the ductility of the DED-L material, is remarkably good.

At room temperature, the strength characteristic values of the DED-L material (see Figure 11) are around 10% lower and most of them less scattered than the ones reported in previous studies





**Figure 11.** Bar charts depicting the characteristic values obtained for the three tested Ti-6Al-4V variants at a) room temperature and b) 400 °C. Values of reference data are also shown (yellow). For the DED-L material, the first column of values at each category represents the results from the tensile test piece on top of the cylinder; the second column from the bottom. The model measurement uncertainty ( $U_M$ ) is shown for selected values as error bars in gray.

that use other local shielding strategies (see data in Table 1). The elongation after fracture (A) is similar to the DED-L material fabricated in argon-flooded process chamber and up to three times higher than the DED-L horizontally deposited (see data in Table 1).<sup>[9,11,12]</sup> Compared with the wrought conventional variants, the yield strength of the DED-L material is only up to 10%, and the ultimate tensile strength only up to 5% lower. The characteristic strength values can be therefore considered similar between all three investigated Ti-6Al-4V variants. The differences in yield strengths can be qualitatively seen in Figure 11. The elongation after fracture is as good as in the wrought variant with equiaxed microstructure and up to three times higher than in the lamellar wrought microstructure. The reduction of area (Z) is, compared with the conventional variant with lamellar microstructure, in average seven times higher in our DED-L material. The difference is less pronounced if

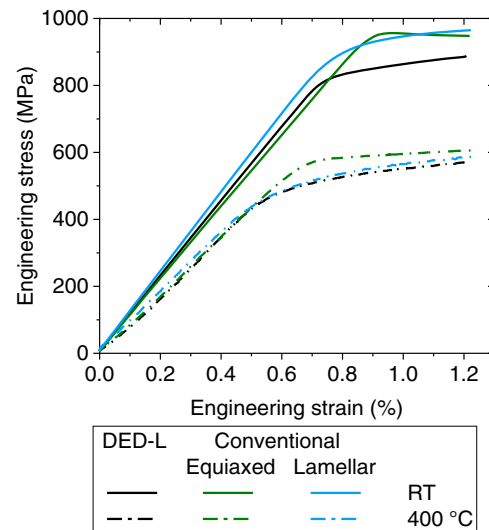


**Figure 12.** Stress-strain curves for the three tested Ti-6Al-4V variants at room temperature (continuous curves) and 400 °C (dashed curves) until removal of the extensometer.

compared with the variant with equiaxed microstructure (around 30% higher).

The trends observed at room temperature, i.e., similar characteristic strength values and, depending on the microstructure comparable to significantly better deformation parameters of the DED-L material compared with the conventional variants, are also observed at 400 °C. The differences in terms of deformation parameters are still considerable at 400 °C but less pronounced. The yield strength of the DED-L material is nearly equal to the one of the wrought variant with lamellar microstructure. The increase in elongation after fracture and reduction of area from room temperature to 400 °C is comparable between the DED-L material and the conventional variant with equiaxed microstructure and of around 25%. In the conventional variant with lamellar microstructure this increase is remarkably higher than that (up to three times). The elastic responses of the DED-L alloy are comparable at both tested temperatures between the three variants investigated (see Figure 12).

The characteristic values of the additively manufactured DED-L material studied are excellent considering the comparison with wrought material since the AM DED-L process without any further heat treatment delivers in principle a casting condition that usually does not come close to the properties of wrought alloys. Overall, the homogeneous microstructure, hardness and strength are an indication of a steady additive build-up process and proves the achieved quality in terms of reproducibility of the properties between single blanks and over the blanks' height.

These excellent results, especially, but not only in terms of ductility, can be discussed by considering the eventually combined effect of different aspects investigated in this study. These include the oxygen content, the thermal or thermomechanical history, and the resulting microstructure. They are all known to affect the ductility and the strength of Ti-6Al-4V.<sup>[2,6,9,12]</sup>

The shielding strategy used in this study leads to very good results in terms of oxygen content (see Table 4). A higher oxygen



content can lead to more propensity to embrittlement, which can negatively impact the ductility. It can also lead to decreased ductility because an interstitial solid solution with Ti is formed at high temperature.<sup>[9]</sup> The interstitial solid solution can also lead to strengthening. Small variations in the oxygen content might lead to variation of the tensile properties. In the work by Carroll et al., the presence of additional oxygen, of the order of 0.0125 wt% in the Ti–6Al–4 V component increased both the ultimate tensile strength and yield strength, and only slightly reduced the ductility.<sup>[12]</sup>

In this study, the oxygen content is similar for all three tested variants (see Table 4), and the DED-L blanks have an oxygen content of 0.17 wt-% (Table 4), which lies between the values of the two reference studies with oxygen contents of 0.2046 and 0.13 wt-%, respectively.<sup>[9,12]</sup> Despite the known and reported dependency of ductility and strength on the oxygen content, the ductility differs between the three variants tested in this study. Besides, the ductility of the DED-L material is higher or similar, and the strength values are lower than in both reference studies. Apart from partially explaining the similarity of the maximum strength values of the three tested variants, a clear correlation of the evaluated properties with the oxygen contents cannot be derived. Therefore, the good quality of the material in terms of oxygen content cannot be considered as the only cause for the excellent properties of the DED-L material. The effect of the microstructure must also be considered.

The different grain sizes, the fineness of the microstructure, e.g., in terms of needle width, the morphology of the prior  $\beta$  grains, and the orientation of the grains related to the loading direction, may also affect the ductility and strength properties.

A fine equiaxed microstructure is known to deliver the best strength and ductility; a coarse lamellar microstructure is at the other extreme.<sup>[2]</sup> This explains the better ductility values of the conventional variant with equiaxed microstructure and the worse ductility of the conventional variant with lamellar microstructure (see Table 4). The excellent ductility of the DED-L material can be partially explained by the fact that in lamellar microstructures, a finer arrangement (smaller lamellae width), which is the case in this study (compare Figure 10d) with Figure 9) is known to deliver better ductility.<sup>[2]</sup> Apart from the fineness of the microstructure, the smaller prior  $\beta$  grain size of the DED-L material and the equiaxed conventional variant, compared to the conventional variant with lamellar microstructure (see Table 5) certainly contributes to their better ductility: the prior  $\beta$  grain size of DED-L Ti–6Al–4 V is only almost half that of the wrought conventional material. The similarity of the maximum strength values of the DED-L with those of the other two tested variants is due to the very fine microstructure of the DED-L material.

Finally, the morphology and orientation of the prior  $\beta$  grains and the existence or not of  $\alpha$  phase at the prior  $\beta$  grain boundaries also have an influence. In the work by Yu et al., the DED-L material has similar grain morphology like our material but is tested perpendicular to the building direction, which potentially explains their low ductility values (see Table 1).<sup>[9]</sup> Carroll et al. reported an anisotropic effect of DED-L Ti–6Al–4 V and attributed it to the elongated grain morphology, which was also similar to the one of our material (see Figure 7).<sup>[12]</sup> They proposed that

the  $\alpha$ -phase at the prior  $\beta$  grain boundaries was subjected to accelerated damage under a tensile opening mode when tension was applied in the longitudinal direction, leading therefore to a lower ductility. The absence of  $\alpha$  at the prior  $\beta$  grain boundaries of the DED-L material might contribute positively to the ductility when compared with the conventional variant with lamellar microstructure (cf. Figure 9 and 10). Furthermore, similar to the results of that study, our study shows that the existence of less grain boundaries perpendicular to the loading direction in the DED-L variant (Figure 7) when compared with the conventional variants (Figure 10) can result in higher ductility values. Less grain boundaries combined with absence of  $\alpha$  at them means less obstacles for the dislocation movement and deformation during the tensile test. This results in a more ductile fracture of the DED-L material that contrasts with the more brittle fracture of the conventional variant with lamellar microstructure after failure, as evidenced by A and Z in Figure 11. The existence of less obstacles for the dislocation movement may also explain its slightly lower yield strength.

The different fracture behaviors become also evident in the fracture surface and on the lateral surfaces of the tensile samples from both materials at both tested temperatures, see Figure 13. Morphologically, the fracture surface in the DED-L tensile samples, Figure 13a,c, as well as in the tensile samples of the conventional variant with equiaxed microstructure (not shown) shows a typical ductile cup-cone like fracture at both tested temperatures. In the conventional variant with lamellar microstructure, Figure 13b,d, the fracture surfaces at both tested temperatures are characteristic of a rather shear-stress dominated failure and the lateral surfaces feature a pronounced surface topography. This failure pattern indicates that the deformation accumulated rather within the grains. The final fracture then presumably occurred under maximum shear stress when the material could no longer accommodate further deformation.

#### 3.4.2. Reproducibility of Properties

To analyze the variation of the properties of the DED-L material along the building height, the model measurement uncertainty ( $U_M$ ) was calculated for  $R_m$ , A, and Z.  $U_M$  is the expanded uncertainty and was determined from the combined uncertainty and a factor  $k=2$ . The combined uncertainty considers the directly incoming sources of uncertainty, i.e., measuring instruments and testing machines. It was calculated according to the UNCERT Code of Practice No. 7.<sup>[45]</sup> The single values are shown as error bars in Figure 11 and available in Table S2, Supporting Information. The percentual differences between the observed individual values of  $R_m$  are for room temperature 1.7% (1006 MPa for top vs 989 MPa for bottom) and for 400 °C 1.9% (689 MPa for top vs 679 MPa for bottom). These values are smaller than all individual values of  $U_M$  ( $\pm 1.2\%$  in all four tests), indicating that the ultimate strength does not vary along the building direction, as it is also the case for the hardness and the microstructure. The latter is also the case for the strength at 400 °C (see Figure 11). The homogeneity of the hardness values within one cylinder (Table 6) supports this finding if considering the positive correlation between  $R_m$  and hardness, as well as the

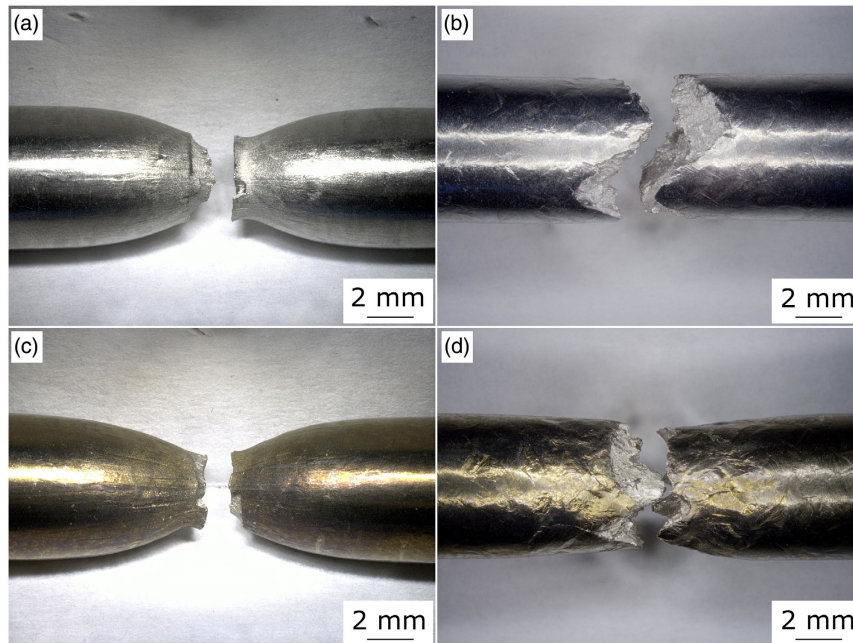


**Figure 13.** a,c) Representative fractured tensile samples of the DED-L material and b,d) of the conventional variant with lamellar microstructure. Tensile samples tested at a,b) room temperature and c,d) at 400 °C.

homogeneity of the microstructure.<sup>[18–20]</sup> This homogeneity of the properties with respect to the building height contrasts the observation of Carroll et al., where location dependency of ultimate tensile and yield strengths at room temperature within the built cruciform was reported.<sup>[12]</sup> The location dependency was there partially attributed to the variance in thermal profile as a function of height that resulted in the presence of a finer microstructure at the bottom of the fabricated wall, resulting in a higher  $R_m$ . The optimized local deposition and shielding and cooling strategy leads in our case to homogeneous properties along the building direction. Furthermore, the homogeneity of the hardness values between the two different blanks and of the microstructure between four different blanks allows deducing that the strength values are representative for all built cylinders. For A and Z at room temperature, the percentage differences between the observed individual values are 12% (A) and 6% (Z). These values are bigger than the biggest  $U_M$  value ( $\pm 1.0\%$  for A on top), These values, in contrast to the tensile strength, vary significantly along the building direction, which may be related to a potential inhomogeneous distribution of defects.

#### 4. Conclusion

In this study, additively manufactured cylindrical DED-L blanks from Ti–6Al–4V fabricated with an optimized deposition and shielding strategy were characterized and benchmarked against literature data. In addition, two conventionally manufactured variants of the same alloy featuring different microstructures were investigated. The relationship between process conditions, resulting microstructure and achieved properties was identified and discussed.

The positive impact of using a combined flow of shielding and carrier gases to form the local protective gas atmosphere in achieving the high quality of the deposited material was highlighted and experimentally proven. The main contribution of the shielding gas is that it increases the gas coverage on the surface and provides additional protection against reaction to atmospheric gases and related embrittlement.

Overall, the DED-L process led to very good mechanical tensile properties at room temperature and at 400 °C. The strength was comparable to all benchmark values. The ductility was very good and similar to the conventional material with equiaxed microstructure. The excellent properties can be explained by considering the combined effect of the low oxygen content and the fine microstructure. The low oxygen content is achieved by the process optimization. Regarding microstructure, the fineness of the needle like microstructure, and the elongated morphology of the prior  $\beta$  grains with absence of  $\alpha$  phase at the grain boundaries, are considered the key distinctive features.

The microstructure, hardness, and tensile strength were proven to be homogeneous between single blanks and with respect to the building height indicating a steady and high qualitative additive build-up process.

#### Supporting Information

Supporting Information is available from the Wiley Online Library or from the author.

#### Acknowledgements

This work was partially funded by the BAM focus area materials project AGIL “Microstructure development in additively manufactured metallic

components: from powder to mechanical failure". The authors thank BAM colleagues Dr. rer. nat. Sebastian Recknagel (BAM-1.6) and Dr.-Ing. Michael Rhode (BAM-9) for performing the measurements of the chemical composition, Oliver Schwarze (BAM-5.3) for performing the density measurements, Christine Krimmling (BAM-5.2) for performing the hardness measurements, and Michelle Fiebig (BAM-5.2), Mareike Kirstein (BAM-9.3), Marina Marten (BAM-9.3), Benjamin Piesker (fmr. BAM-5.2), Kathrin Ohm (BAM-9.1), and Leon Domroese (fmr. BAM-5.2) for their collaboration in metallography and optical microscopy.

Open access funding enabled and organized by Projekt DEAL.

## Conflict of Interest

The authors declare no conflict of interest.

## Data Availability Statement

The raw/processed data required to reproduce these findings cannot be shared at this time as the data also forms part of an ongoing study.

## Keywords

laser powder-based directed energy deposition, local protective gas atmosphere, microstructure, tensile properties, Ti-6Al-4V

Received: September 29, 2021

Revised: December 15, 2021

Published online:

- [1] J. O. Milewski, in: *Additive Manufacturing of Metals*, Springer Series in Materials Science, Vol. 258, Springer Cham **2017**.
- [2] M. Peters, C. Leyens, *Titanium and titanium Alloys: Fundamentals and Applications*, Wiley, Hoboken, NJ **2003**.
- [3] F. H. Froes, M. Qian, *Titanium in Medical and Dental Applications*, Woodhead Publishing, Swanton, Cambridge **2018**.
- [4] T. DebRoy, H. L. Wei, J. S. Zuback, T. Mukherjee, J. W. Elmer, J. O. Milewski, A. M. Beese, A. Wilson-Heid, A. De, W. Zhang, *Prog. Mater. Sci.* **2018**, 92, 112.
- [5] S. Liu, Y. C. Shin, *Mater. Des.* **2019**, 164, 107552.
- [6] R. Boyer, G. Welsch, E. W. Collings, *Materials Properties Handbook: Titanium Alloys*, ASM International, Almere, The Netherlands **1994**.
- [7] Y. Xia, J. Zhao, Q. Tian, X. Guo, *JOM* **2019**, 71, 3209.
- [8] K. Bungardt, K. Rüdinger, *Int. J. Mater. Res.* **1956**, 47, 585.
- [9] J. Yu, M. Rombouts, G. Maes, F. Motmans, *Phys. Proc.* **2012**, 39, 416.
- [10] F. Spranger, B. Graf, M. Schuch, K. Hilgenberg, M. Rethmeier, *J. Laser Appl.* **2018**, 30, <https://doi.org/10.2351/1.4997852>.
- [11] A. M. Beese, B. E. Carroll, *JOM* **2016**, 68, 724.
- [12] B. E. Carroll, T. A. Palmer, A. M. Beese, *Acta Mater.* **2015**, 87, 309.
- [13] A. W. Bowen, C. A. Stubbington, in *Titanium and Titanium Alloys: Scientific and Technological Aspects*, Vol. 3, Springer US, Boston, MA, **1982**, p. 1989.
- [14] J. N. Montero, A. Rodríguez, J. M. Amado, M. J. Tobar, A. Yáñez, presented at *Lasers Manufacturing Conf.*, Munich, Germany, June 2015.
- [15] DIN EN 3312:2012-05 Aerospace Series – Titanium Alloy Ti-6Al-4V – Annealed – Forgings – De $\leq$ 150 mm, Deutsches Institut für Normung e. V. (DIN), Beuth Verlag, Berlin **2012**.
- [16] ASTM B348/B348M-19, Standard Specification for Titanium and Titanium Alloy Bars and Billets, ASTM International, West Conshohocken, PA **2019**.
- [17] A. Eder, M. Jordan, in *Optical Measurements. Heat and Mass Transfer*, (Eds: F. Mayinger, O. Feldmann), Springer, Berlin, Heidelberg **2001**.
- [18] DIN EN ISO 18265:2014-02: Metallic Materials – Conversion of Hardness Values, Deutsches Institut für Normung e. V., Berlin **2014**.
- [19] J. M. Oh, B. G. Lee, S. W. Cho, S. W. Lee, G. S. Choi, J. W. Lim, *Metals Mater. Int.* **2011**, 17, 733.
- [20] D. J. Abson, F. J. Gurney, *Metals Technol.* **1974**, 1, 483.
- [21] C. Rueden, K. Eliceiri, *BMC Bioinform.* **2017**, 18, 529.
- [22] DIN EN ISO 1183-2 Plastics – Methods for Determining the Density of Non-Cellular Plastics – Part 2: Density Gradient Column Method, Deutsches Institut für Normung e. V., Beuth Verlag, Berlin **2019**.
- [23] DIN EN ISO 6507-1: 2018-07 Metallic Materials – Vickers Hardness Test – Part 1: Test Method, Deutsches Institut für Normung e. V. (DIN), Beuth Verlag, Berlin **2018**.
- [24] Material Datasheet Titan Grade 5, <https://www.thyssenkrupp-materials.ch/de/downloads/werkstoffdatenblaetter-titan>, (accessed: February 2018).
- [25] DIN 50125:2016-12 Testing of Metallic Materials – Tensile Test Pieces, Deutsches Institut für Normung e. V., Beuth Verlag, Berlin **2016**.
- [26] DIN EN ISO 6892-1:2017-02 Metallic Materials – Tensile Testing Part 1: Method of Test at Room Temperature, Deutsches Institut für Normung e. V. (DIN), Beuth Verlag, Berlin **2017**.
- [27] DIN EN ISO 6892-2: 2018-09 Metallic Materials – Tensile Testing – Part 2: Method of Test at Elevated Temperature, Deutsches Institut für Normung e. V. (DIN), Beuth Verlag, Berlin **2018**.
- [28] Guideline DVS 2713 (04/2016). Welding of Titanium Materials, Processes, Manufacture, Inspection and Evaluation of Weld Joints with Supplementary Sheet, DVS, Technical Committee, Working Group "Welding in Aviation and Aerospace Engine", Düsseldorf **2016**.
- [29] M. Yan, W. Xu, M. S. Dargusch, H. P. Tang, M. Brandt, M. Qian, *Powder Metall.* **2014**, 57, 251.
- [30] M. Neikter, P. Åkerfeldt, R. Pederson, M-L. Antti, *IOP Conf. Ser. Mater. Sci. Eng.* **2017**, 258, 012007.
- [31] T. Ahmed, H. J. Rack, *Mater. Sci. Eng. A* **1998**, 243, 206.
- [32] ASTM E112-13 Standard Test Methods for Determining Average Grain Size, ASTM International, West Conshohocken, PA **2013**.
- [33] DIN EN ISO 643:2013-05 Steel – Microphotographic Determination of the Apparent Grain Size, Deutsches Institut für Normung e. V. (DIN), Beuth Verlag, Berlin **2013**.
- [34] T. Mukherjee, J. S. Zuback, A. De, T. DebRoy, *Nat. Sci. Rep.* **2016**, 6, 1.
- [35] A. Dass, A. Moridi, *Coatings* **2019**, 9, 418.
- [36] D. Chioibas, S. Mihai, M. A. Mahmood, M. Lungu, I. Porosnicu, A. Sima, C. Dobrea, I. Tiseanu, A. C. Popescu, *Metals* **2020**, 10, 1408.
- [37] T. Mishurova, K. Artzt, J. Haubrich, G. Requena, G. Bruno, *Addit. Manufact.* **2019**, 25, 325.
- [38] S. Muzon, T. Mishurova, S. Evsevlev, S. Dubiez-Le Goff, S. Murugesan, G. Bruno, E. Hryha, *Addit. Manufact.* **2021**, 47, 102340.
- [39] T. Petrat, C. Brunner-Schwer, B. Graf, M. Rethmeier, *Proc. Manufact.* **2019**, 36, 256.
- [40] I. Polmear, D. StJohn, J-F. Nie, M. Qian, in *Light Alloys 5th ed.*, Butterworth-Heinemann, Boston **2017**, p. 369.
- [41] H. Ali, H. Ghadbeigi, K. Mumtaz, *Mater. Sci. Eng. A-Struct.* **2018**, 712, 175.
- [42] F. Z. Li, Z. Wang, X. Y. Zeng, *Mater. Lett.* **2017**, 199, 79.
- [43] T. Vilaro, C. Colin, J. D. Bartout, *Metall. Mater. Trans. A* **2011**, 42a, 3190.
- [44] J. Kim, K-H. Kim, D. Kwon, *Metals Mater. Int.* **2016**, 22, 209.
- [45] W. Gabauer, The Determination of Uncertainties in Tensile Testing, UNCERT COP 07:2000 Manual of Codes of Practice for the Determination of Uncertainties in Mechanical Tests on Metallic Materials, Code of Practice No. 07, Austria, **2000**.